Facile Synthesis of Manganese-Oxide-Containing Mesoporous Nitrogen-Doped Carbon for Efficient Oxygen Reduction

Yueming Tan, Chaofa Xu, Guangxu Chen, Xiaoliang Fang, Nanfeng Zheng, and Qingji Xie*

Developing low-cost non-precious metal catalysts for high-performance oxygen reduction reaction (ORR) is highly desirable. Here a facile, in situ template synthesis of a MnO-containing mesoporous nitrogen-doped carbon (*m*-N-C) nanocomposite and its high electrocatalytic activity for a four-electron ORR in alkaline solution are reported. The synthesis of the MnO-*m*-N-C nanocomposite involves one-pot hydrothermal synthesis of Mn_3O_4@polyaniline core/shell nanoparticles from a mixture containing aniline, $Mn(NO_3)_2$, and $KMnO_4$, followed by heat treatment to produce N-doped ultrathin graphitic carbon coated MnO hybrids and partial acid leaching of MnO. The as-prepared MnO-*m*-N-C composite catalyst exhibits high electrocatalytic activity and dominant four-electron oxygen reduction pathway in 0.1 M KOH aqueous solution due to the synergetic effect between MnO and *m*-N-C. The pristine MnO shows little electrocatalytic activity and *m*-N-C alone exhibits a dominant two-electron process for ORR. The MnO-*m*-N-C composite catalyst also exhibits superior stability and methanol tolerance to a commercial Pt/C catalyst, making the composite a promising cathode catalyst for alkaline methanol fuel cell applications. The synergetic effect between MnO and N-doped carbon described provides a new route to design advanced catalysts for energy conversion.

1. Introduction

Electrochemical energy conversion devices, ranging from fuel cells to metal-air batteries, require effective electrocatalysts for oxygen reduction reaction (ORR).[1–4] Pt and its alloys with well controlled facets are well known as active and efficient catalysts for ORR,[5–8] but their high cost, limited supply, and weak durability severely hinder their applicability to broad commercialization. One solution to overcome this predicament is to replace the Pt-based catalysts with non-precious metal catalysts for ORR.[9–16] Therefore, the development of non-precious metal catalysts with comparable ORR activity to Pt-based catalysts but with higher durability and much lower cost is highly desirable.

Currently, N-doped carbon materials are extensively demonstrated as a potential substitute for Pt to reduce the cost and enhance the stability of ORR electrocatalysts.[17–21] The incorporation of N element into carbon materials can significantly enhance the number of active sites for improved ORR activity. For instance, N-doped carbon nanotube arrays show excellent electrocatalytic activity for ORR in air-saturated 0.1 M potassium hydroxide.[17] However, the ORR activities of most N-doped carbons are still on a less competitive level compared to Pt catalysts. One of the drawbacks of these catalysts is the limited surface area, resulting in limited catalytic sites exposed to oxygen molecules.[22–24] Mesoporous N-doped carbon (*m*-N-C) can largely increase the surface area and thus enhance the ORR activity.[24] Despite the great efforts, *m*-N-C calalysts still exhibit a much lower mass/volume activity compared with Pt-based materials. Moreover, some *m*-N-C calalysts usually undergo two-electron oxygen reduction pathway,[25] which limits the electrocatalytic efficiency for ORR. In addition, peroxide generation during two-electron oxygen reduction process can severely reduce the stability of ORR catalyst.[26] Hence, it is still important to develop new strategy to further improve the ORR activities of *m*-N-C catalysts and prevent them from generating peroxide.

In the past decades, various manganese oxides (MnO_x), including MnO_2, MnO, Mn_2O_3, Mn_3O_4, Mn_5O_8, MnOOH, and amorphous MnO_x have also been widely studied as alternative ORR catalysts in alkaline solutions, because of their low cost and minimum environmental impact.[27–33] However, pristine MnO_x usually exhibits limited ORR activities probably due to

---

Y. M. Tan, C. F. Xu, G. X. Chen,
X. L. Fang, Prof. N. F. Zheng
State Key Laboratory for Physical Chemistry
of Solid Surfaces and Department of Chemistry
College of Chemistry and Chemical Engineering
Xiamen University
Xiamen 361005, China
E-mail: nfzheng@xmu.edu.cn
Prof. Q. J. Xie
Key Laboratory of Chemical Biology and Traditional
Chinese Medicine Research (Ministry of Education of China)
College of Chemistry and Chemical Engineering
Hunan Normal University
Changsha 410081, China

DOI: 10.1002/adfm.201201244

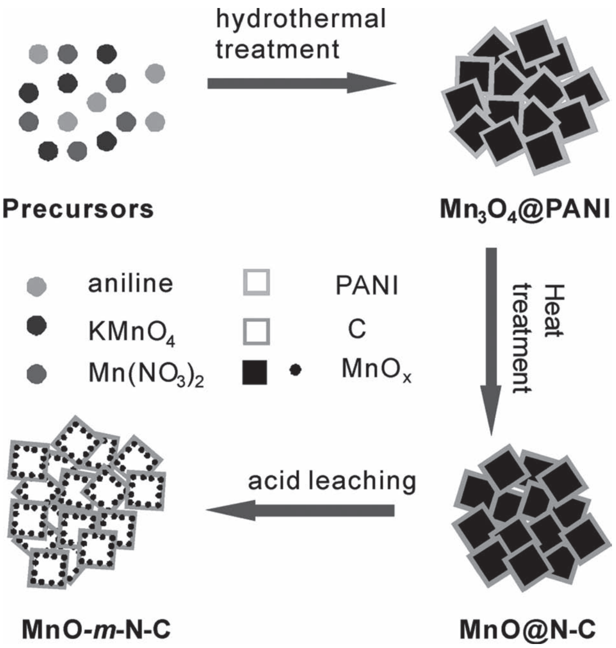

Scheme 1. Illustration of the synthetic procedure for the MnO-*m*-N-C nanocomposite.

their low electrical conductivity. Loading of MnO_x on conducting carbon carriers can overcome the limitation and improve the ORR activity. For instance, a composite air electrode consisting of Ketjen Black carbon supported amorphous MnO_x nanowires, synthesized via a polyol method, is highly efficient for the ORR in a Zn-air battery.[28] Considering that both N-doped carbons and MnO_x have considerable ORR activities, it is interesting to study the synergetic coupling effect between the low-cost MnO_x and polymer-derived N-doped carbons (especially *m*-N-C) for ORR, though the effects of incorporation of Fe, Co, and their oxides in N-doped carbons on ORR activities have been widely studied.[34–38]

Herein, a novel, in situ MnO_x-template method was developed to prepare MnO-containing *m*-N-C nanocomposite that displays high electrocatalytic activity for a four-electron ORR in alkaline solution. The content of N component in the MnO-*m*-N-C nanocomposite is as high as ≈5 wt% at optimized MnO content of 35 wt%. The MnO-*m*-N-C nanocomposite has a high surface area of 236 m^2 g^{-1} resulting from the mesoporous structure. Due to the unique structure and composition, the MnO-*m*-N-C composite catalyst shows similar electrocatalytic activity but superior stability and methanol tolerance to commercial Pt/C catalyst for four-electron ORR in alkaline solution, indicating a promising cathode catalyst candidate for alkaline methanol fuel cell applications.

2. Results and Discussion

As shown in **Scheme 1**, the synthesis of MnO-*m*-N-C involves one-pot hydrothermal synthesis of Mn_3O_4@polyaniline (PANI) core-shell nanoparticles, followed by heat treatment to yield ultrathin nitrogen-doped graphitic carbon coated MnO hybrids, and then partial acid leaching of MnO. In the first step, Mn_3O_4@PANI core-shell nanoparticles were synthesized by one-pot hydrothermal treatment of a mixture containing aniline, $Mn(NO_3)_2$, and $KMnO_4$. The morphologies of the prepared Mn_3O_4@PANI composites were examined by transmission electron microscopy (TEM). As shown in **Figure 1**a–c, the nanoparticles with an average diameter of ≈20 nm are coated uniformly with a ≈2 nm-thick polymer layer. The corresponding X-ray diffraction (XRD) pattern is shown in Figure 1g and the peaks can be assigned to the hausmannite Mn_3O_4 (JCPDS 24-0734) phase. After heat treatment at 900 °C under Ar atmosphere for 4 h, an ultrathin graphitic carbon shell (≈1 nm) can be observed on the nanoparticles (Figure 1d–f). The curved lattice fringes clearly show graphitic (002) layers with an interplanar spacing of 0.33 nm (Figure 2f). The distortion of circular stripes should be attributed to defects formed during the graphitization process. The XRD result revealed that annealed Mn_3O_4 nanoparticles were completely converted into MnO (JCPDS 75-0626) in the inert atmosphere (Figure 1h). The as-prepared ultrathin graphitic carbon coated MnO hybrids were etched in 0.1 M H_2SO_4 for 24 h to yield the MnO-*m*-N-C nanocomposite. As shown in **Figure 2**, mesoporous carbons with MnO adhering to the ultrathin graphitic carbon shell can be observed. It is worth noting that a small number of large MnO nanoparticles still exist after acid leaching (labeled by arrows in Figure 2a,b). Due to their rather small size and low electron contrast, the fine MnO particles adhered to the carbon shells are barely observed by low-magnification TEM but can be clearly identified by HRTEM. Their size is typically less than 5 nm. The XRD result also clearly revealed that the as-prepared MnO-*m*-N-C nanocomposite consists of MnO and graphitic carbon. As shown in Figure 2d, the peaks at 35.0°, 40.6°, 58.8°, and 70.3° are in good agreement with (111), (200), (220), and (311) planes of the cubic MnO, respectively. A strong peak observed at 26.0° can be attributed to the (002) plane of the hexagonal graphite structure, suggesting the presence of highly graphitic carbon. As well known, the graphitization of the carbons in the catalysts can enhance the electronic conductivity and corrosion resistance of the carbon-based catalysts during electrocatalysis.[34,39] Thermogravimetric analysis (TGA) results also indicate that some MnO component still remained in the mesoporous carbon shells. As shown in Figure S1 (Supporting information), due to the decomposition of carbon shells during thermal decomposition process under air atmosphere, the MnO-*m*-N-C nanocomposite exhibits 62% mass loss. The involvement of N element in the carbon shells was verified by element analysis. As listed in Table S1 (Supporting Information), the weight ratio between C and N is 11.8:1, indicating the efficient incorporation of N element into the carbon matrix. The content of N component is still as high as ≈5 wt%, though the content of MnO in the MnO-*m*-N-C nanocomposite reaches almost 35 wt%. There is a small discrepancy in the content of MnO between element analysis data and TGA result, because the involved MnO in the carbon shells can be converted to Mn_3O_4 during TGA measurement thereby leading to mass increase. In fact, the involved MnO can be etched completely in 1 M H_2SO_4 aqueous solution for 72 h yielding pristine mesoporous graphitic carbon. Thus, we have developed a simple and efficient approach to prepare mesoporous carbon and metal oxide-containing mesoporous carbon.

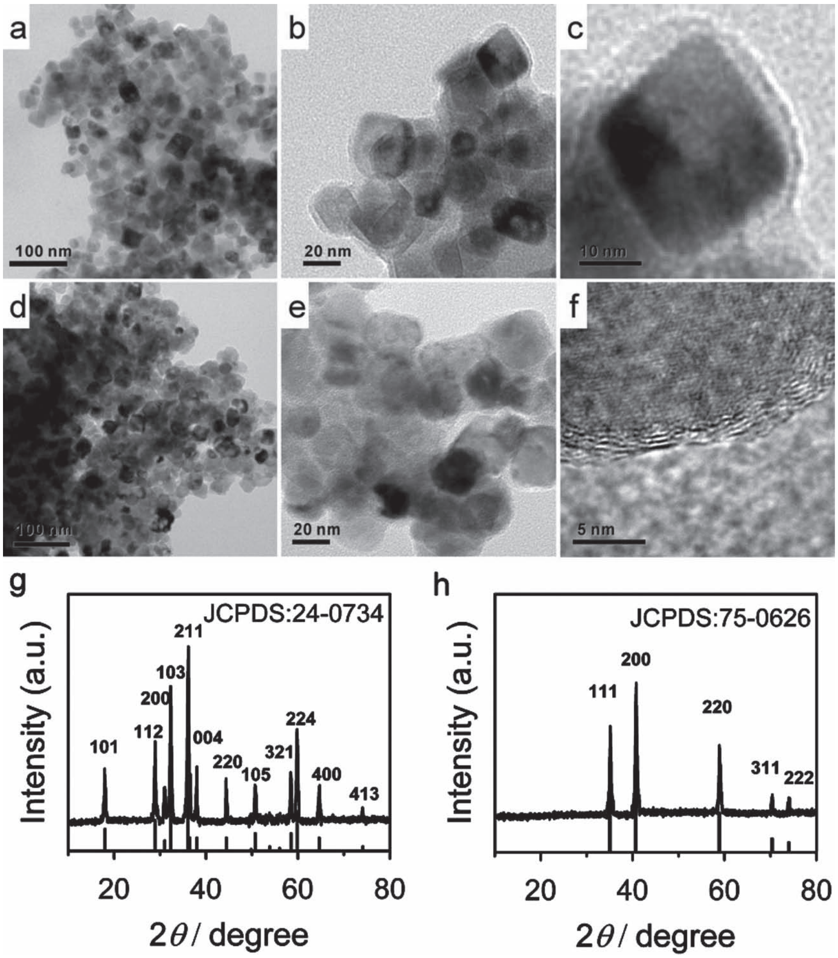

Figure 1. a–f) TEM images of Mn_3O_4@PANI (a–c) and MnO@C (d–f) nanoparticles at different magnifications. g,h) XRD patterns of Mn_3O_4@PANI (g) and MnO@C (h) nanoparticles.

Figure 2d shows the nitrogen adsorption-desorption isotherms and pore size distribution of the MnO-*m*-N-C nanocomposite. The MnO-*m*-N-C nanocomposite shows a high BET surface area of 236 m^2 g^{-1}. A distinct hysteresis loop can be observed in the larger range of ca. 0.45–1.0 P/P_0, indicating the presence of a mesoporous structure. The pore size distribution, calculated from desorption data using the BJH model, was evaluated to have an average value of ≈13 nm, which is very consistent with the TEM results. It is obvious that the high specific surface area is mainly attributed to the formation of a mesoporous structure. The high surface area of the MnO-*m*-N-C nanocomposite should provide surface density of catalytic sites exposed to oxygen molecules and thus result in ORR activity enhancement. In addition, the mesoporous structure can also provide the possibility of efficient mass transport and thus lead to enhanced electrocatalytic performance.[24,40,41]

To better compare and understand the ORR performance of MnO-m-N-C nanocomposite, *m*-N-C and pristine MnO nanoparticles were also prepared (see experimental section for details) and used as reference catalysts. The *m*-N-C shows the similar morphology as MnO-*m*-N-C except for the absence of MnO (Figure S2, Supporting Information). The *m*-N-C has a high BET surface area of 748 m^2 g^{-1} and an average pore size ≈12 nm. TEM and XRD patterns of pristine MnO nanoparticles reveals that the as-prepared pristine MnO nanoparticles are pure MnO phase. The average size of MnO nanoparticles calculated through the Scherrer's equation by analyzing the XRD diffraction peaks is ≈23 nm (Figure S3, Supporting Information). The MnO-*m*-N-C nanocomposite was tested as electrocatalyst for ORR in 0.1 M KOH aqueous solution. **Figure 3** shows the cyclic voltammograms of MnO-*m*-N-C, *m*-N-C, MnO, and physical mixture of *m*-N-C and MnO nanoparticles (wt/wt = 6:4) catalysts in O_2-saturated and N_2-saturated 0.1 M KOH solution. The MnO catalyst shows a cathodic peak at 0.56 V, and the *m*-N-C catalyst shows a cathodic peak at 0.75 V. In contrast, the MnO-*m*-N-C composite catalyst shows a much more positive cathodic peak at 0.82 V and higher cathodic current, suggesting synergetic ORR catalytic activity of MnO and *m*-N-C in the nanocomposite. The cathodic peak potential for MnO-*m*-N-C composite catalyst is more positive than that for manganese-based and N-doped carbon-based electrocatalysts reported previously (typically negative than 0.75 V),[24,27,32,40,42] highlighting low overpotential for ORR and excellent oxygen reduction ability of MnO-*m*-N-C composite catalyst. Interestingly, the cathodic peak potential for MnO-*m*-N-C composite catalyst is higher than that for physical mixture of *m*-N-C and MnO catalyst (0.77 V), suggesting a better synergetic coupling between MnO and N-doped carbon in the MnO-*m*-N-C composite catalyst.

The ORR measurements were performed in O_2-saturated 0.1 M KOH aqueous solution at room temperature by using a rotating disk electrode (RDE). A characteristic set of polarization curves for the ORR on MnO-*m*-N-C, *m*-N-C, MnO, physical mixture of *m*-N-C and MnO, and commercial Pt/C (20 wt% Pt, E-TEK) catalysts modified RDEs are displayed in **Figure 4**a. The pristine MnO catalyst exhibits little ORR activity. The RDE polarization curves show that the MnO-*m*-N-C composite catalyst has an onset potential more positive than *m*-N-C, MnO, and physical mixture of *m*-N-C and MnO catalysts. As shown in Figure 4b, the half-wave potential ($E_{1/2}$) of MnO-*m*-N-C composite catalyst is 0.81 V, which is more positive than that of *m*-N-C (0.73 V), MnO (0.61 V), and physical mixture of *m*-N-C and MnO (0.75 V) catalysts, and only 50-mV negative shift compared with Pt/C catalyst (0.86 V). The half-wave potential of MnO-*m*-N-C composite catalyst is more positive than that of some non-precious metal electrocatalysts reported previously in 0.1 M KOH solution (typically negative than 0.80 V),[10–12,24,28,33,40–42] highlighting the high ORR activity of MnO-*m*-N-C composite catalyst. In addition, the diffusion-limiting current of MnO-*m*-N-C composite catalyst is almost comparable with that of Pt/C catalyst, and much higher than that of *m*-N-C,

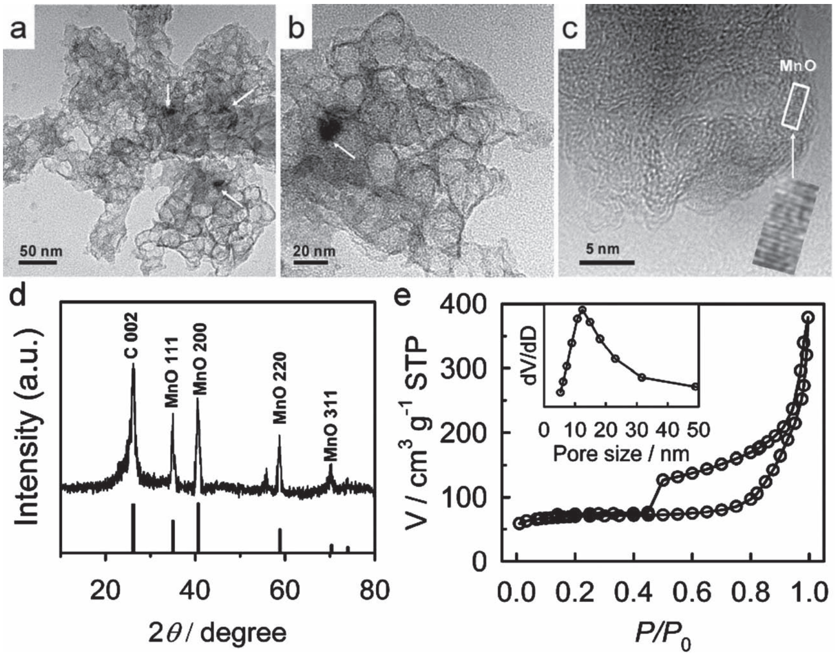

Figure 2. a–c) TEM images of MnO-*m*-N-C nanocomposite at different magnifications. d) XRD pattern of MnO-*m*-N-C nanocomposite. Arrows in (a,b) indicate that a small number of large MnO nanoparticles exist in the catalyst. The inset of (c) is an enlarged image taken from the corresponding white boxed area. e) Nitrogen adsorption and desorption isotherms of MnO-*m*-N-C nanocomposite. Inset shows pore size distribution curve.

MnO, and physical mixture of *m*-N-C and MnO catalysts. The higher half-wave potential and larger diffusion-limiting current of MnO-*m*-N-C composite catalyst than those of *m*-N-C, MnO, and physical mixture of *m*-N-C and MnO catalysts should also suggest the existence of synergetic effect between MnO and *m*-N-C in the nanocomposite. A set of polarization curves for the ORR on MnO-*m*-N-C composite catalyst recorded from 400 to 2500 rpm are displayed in Figure 4c. These polarization curves show typical increasing current with higher rotation speeds, which can be explained by shortened diffusion distance at high speeds. The Koutecky–Levich plots (j^{-1} vs. $\omega^{-1/2}$) are obtained from polarization curves at different potentials (Figure 4d). The linearity of the Koutecky-Levich plots and near parallelism of the fitting lines suggests first-order reaction kinetics toward the concentration of dissolved oxygen and similar electron transfer number for ORR at different potentials.[37] The electron transfer number (n) from the slopes of Koutecky-Levich plots is calculated to be 3.84 at potentials from 0.45 to 0.65 V, suggesting that MnO-*m*-N-C composite catalyst exhibits dominant four-electron oxygen reduction process, similar to ORR catalyzed by commercial Pt/C catalyst (Figure S4, Supporting Information). However, *m*-N-C alone without MnO exhibits the electron transfer number of 2.56–2.65 depending on the potentials (Figure S5, Supporting Information), indicating a combined two-electron and four-electron reaction pathway.

To verify the ORR catalytic pathways of these catalysts, rotating ring-disk electrode (RRDE) measurements were carried out to monitor the formation of peroxide species (HO_2^-) during the ORR process. As shown in **Figure 5**, the produced HO_2^- for the MnO-*m*-N-C composite catalyst is below 11% and the corresponding electron transfer number is calculated to ≈3.8 over the potential range of 0.35–0.85 V, well consistent with the result obtained from the Koutecky-Levich plots based on RDE measurements. In contrast, the *m*-N-C catalyst produced 65–73% HO_2^- and the value of electron transfer number is 2.52–2.72 over the potential range of 0.35–0.85 V, indicating that *m*-N-C catalyst exhibits dominant two-electron reaction process though it possess considerable ORR activity.

To understand the mechanism of high electrocatalytic activity and dominant four-electron oxygen reduction process with the MnO-*m*-N-C composite catalyst, the produced HO_2^- for physical mixture of *m*-N-C and MnO catalyst was also monitored (Figure 5). Interestingly, the physical mixture of *m*-N-C and MnO nanoparticles exhibits lower HO_2^- yield and higher electron transfer number than *m*-N-C catalyst alone at potentials lower than 0.85 V. The electrocatalytic performance of pristine MnO catalyst toward peroxide was also evaluated. Figure S6 (Supporting Information) shows the cyclic voltammograms of MnO catalyst in 0.1 M KOH aqueous solution in the absence and presence of 1 mM H_2O_2. In the presence of H_2O_2, the

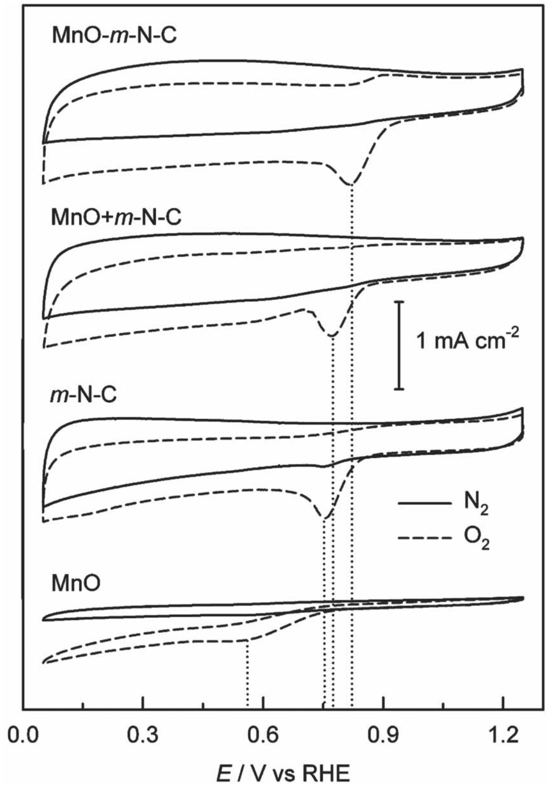

Figure 3. Cyclic voltammograms of MnO-*m*-N-C, *m*-N-C, and MnO, and physical mixture of *m*-N-C and MnO catalysts in O_2-saturated (dashed curves) and N_2-saturated 0.1 M KOH (solid curves).

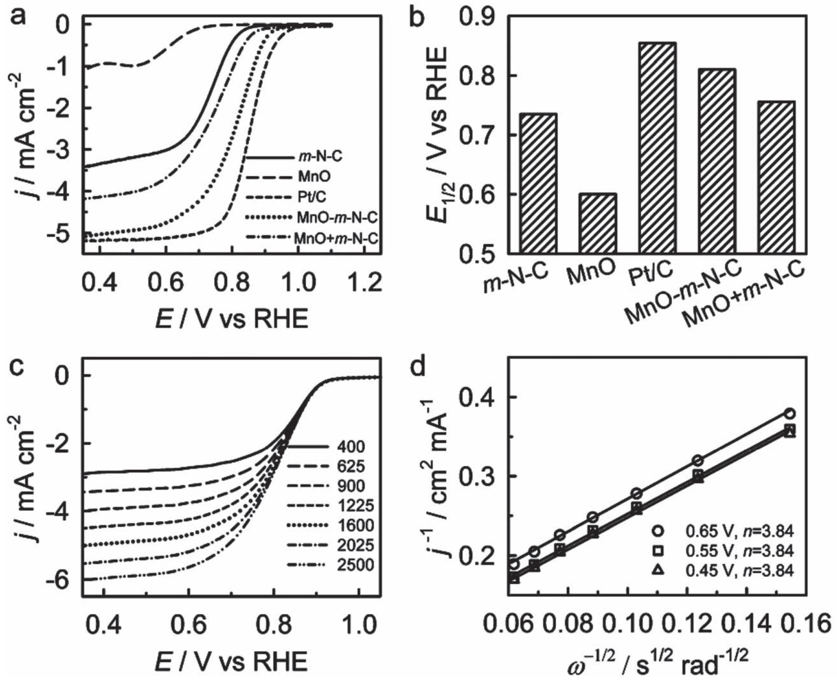

Figure 4. a) ORR polarization curves for MnO-*m*-N-C, *m*-N-C, MnO, Pt/C, and physical mixture of *m*-N-C and MnO catalysts recorded in an O_2-saturated 0.1 M KOH aqueous solution at a sweep rate of 5 mV s^{-1} and a rotation rate of 1,600 rpm. b) Half-wave potentials ($E_{1/2}$) of these catalysts. c) ORR polarization curves for MnO-*m*-N-C catalyst at the different rotation rates indicated. d) Koutecky-Levich plots for MnO-*m*-N-C catalyst at different potentials.

MnO catalyst shows increased cathodic current at potentials lower than 0.85 V, indicating that pristine MnO catalyst has considerable electrocatalytic activity toward peroxide. Therefore, the enhanced electrocatalytic performance for physical mixture of *m*-N-C and MnO nanoparticles compared to *m*-N-C alone may be explained as follows,

$$O_2 + H_2O + 2e^- \xrightarrow{m\text{-N-C}} HO_2^- + OH^-$$

$$HO_2^- + H_2O + 2e^- \xrightarrow{\text{MnO}} 3OH^-$$

Namely, oxygen molecule is reduced to peroxide at N-C sites and further reduced to OH^- at adjacent MnO sites. In fact, a dual-site mechanism has been proposed for cobalt-polypyrrole/C ORR catalyst, in which oxygen is reduced to peroxide at Co-N-C sites and further reduced to OH^- at Co_xO_y/Co sites.[43] However, the electrocatalytic performance for physical mixture of *m*-N-C and MnO nanoparticles is much worse than that for MnO-*m*-N-C composite catalyst, highlighting the advantage of the unique structure of MnO-*m*-N-C composite catalyst. In fact, the electrocatalysis for MnO-*m*-N-C composite catalyst mainly occurs in the hollow carbon shells, so the produced intermediate HO_2^- can be captured efficiently by MnO nanoparticles encapsulated in the carbon shells. In addition, the MnO nanoparticles directly adhering to the carbon shell in MnO-*m*-N-C nanocomposite can facilitate fast electron transfer.[28] Recently, it has been reported that the interactions between Co_3O_4 and N-doped graphene for Co_3O_4/graphene catalyst can lead to improved ORR activity.[37] A similar mechanism may also work in our MnO/ultrathin N-doped graphitized carbon hybrid system. We believe that the tight interaction between MnO and N-doped graphitized carbon in the MnO-*m*-N-C composite catalyst significantly contributes to the observed synergetic effect and enhanced ORR performance.

The high surface area of MnO-*m*-N-C nanocomposite resulting from the mesoporous structure also makes a remarkable contribution to the ORR activity enhancement. The MnO-C hybrids were etched in 0.1 M H_2SO_4 aqueous solution for different time. As revealed by the TGA data (Figure S7, Supporting Information), more MnO components were removed with increasing periods of leaching. Figure S8 (Supporting Information) shows the ORR

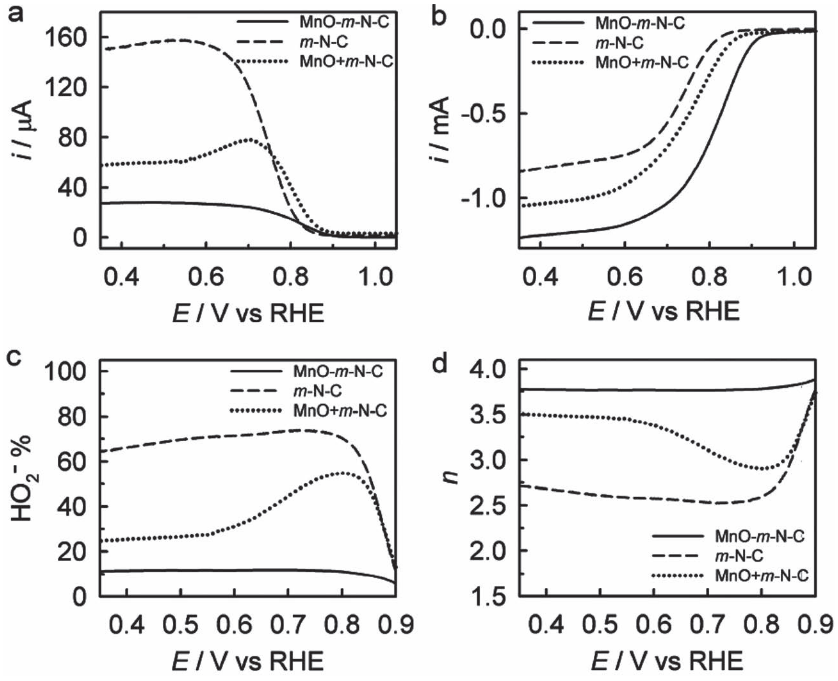

Figure 5. a) Ring current and b) disk current of MnO-*m*-N-C, *m*-N-C, and physical mixture of *m*-N-C and MnO catalysts obtained from the rotating ring-disk electrode measurements in O_2-saturated 0.1 M KOH at a sweep rate of 5 mV s^{-1} and a rotation rate of 1600 rpm. c) Percentage of peroxide and d) the electron transfer number of these catalysts at various potentials.

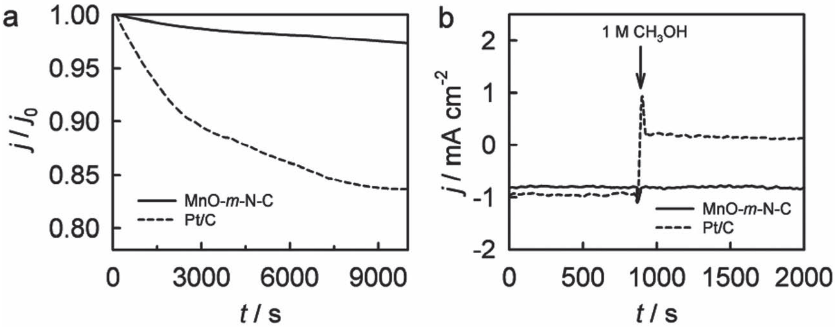

Figure 6. a) Chronoamperometric responses of MnO-*m*-N-C and Pt/C catalysts at 0.75 V in O_2-saturated 0.1 M KOH, which are normalized to the initial current responses. b) Chronoamperometric responses to injection of 1 M methanol into O_2-saturated 0.1 M KOH solution at MnO-*m*-N-C and Pt/C catalysts modified electrodes.

polarization curves and Tafel plots for MnO-C hybrids after acid leaching for different time. Highest diffusion-limiting current and lowest Tafel slope at low overpotential region are observed for the MnO-*m*-N-C nanocomposite prepared by acid leaching for 24 h, indicating the highest ORR activity for MnO-*m*-N-C. Obviously, with the increase of leaching time from 0 to 24 h, MnO-containing N-doped carbons with increased surface area were obtained. The higher surface area can provide more catalytic sites exposed to oxygen molecules and thus result in ORR activity enhancement. However, most MnO components were removed after acid leaching for 72 h, which would weaken the synergetic effect between MnO and *m*-N-C and thus lead to negative-shift of the onset potential and decrease of the diffusion-limiting current.

The durability of MnO-*m*-N-C and Pt/C catalysts toward ORR was evaluated through chronoamperometric measurements at 0.75 V. As shown in **Figure 6**a, the 10 000 s test only caused a slight activity loss on MnO-*m*-N-C catalyst, whereas Pt/C lost nearly 17% of its initial activity. These results indicate a much better stability of MnO-*m*-N-C catalyst than commercial Pt/C catalyst in alkaline solution, which is favored for the development of alkaline fuel cells. The stability of non-precious metal catalysts has been frequently correlated with the amount of peroxide releasing during the ORR.[26] Since the MnO-*m*-N-C catalyst exhibits a nearly four-electron oxygen reduction pathway for the ORR, it is not surprising that the catalyst has excellent durability. An excellent catalytic selectivity for cathode reactions against fuel oxidation is important for an efficient ORR electrocatalyst for fuel cell application, especially when using small-molecule organic fuels, such as methanol, which could cross over through the polymer electrolyte membrane from anode to cathode, seriously compromising the whole cell performance.[44–49] Both MnO-*m*-N-C and Pt/C catalysts were further subjected to testing the possible crossover in the presence of 1 M methanol. After adding methanol to the electrolyte, MnO-*m*-N-C catalyst retained stable current response whereas the current responses for Pt/C catalyst instantaneously jumped to positive values owing to occurrence of methanol oxidation reaction on Pt/C catalyst. These results clearly show the better catalytic selectivity of MnO-*m*-N-C catalyst and its better suitability as a cathode catalyst for alkaline methanol fuel cell than the commercial Pt/C catalyst.

3. Conclusions

In summary, novel MnO-*m*-N-C nanocomposite was facilely synthesized without additional template. Throughout the synthesis process and electrocatalysis, manganese oxides play very important roles, including serving as a template for carbon coating and synergetic active sites for ORR. Due to the synergetic effects between MnO and *m*-N-C, the MnO-*m*-C composite catalyst exhibits high ORR activity in alkaline solution. The high surface area of the MnO-*m*-N-C nanocomposite resulting from the mesoporous structure also make a remarkable contribution to high ORR activity. In addition to the excellent electrocatalytic activity, the as prepared MnO-*m*-C composite catalyst exhibits superior stability and methanol tolerance to commercial Pt/C catalyst for ORR, indicating a promising cathode catalyst candidate for alkaline methanol fuel cell applications. The novel synthesis method described here may be extended to the preparation of many other kinds of mesoporous carbons or metal oxides-containing mesoporous carbons for wide applications including energy storage, catalysis, and electrocatalysis.

4. Experimental Section

Instrumentation and Chemicals: Electrochemical experiments were conducted on a CHI760D electrochemical workstation (CH Instrument Co., USA). A conventional three-electrode system included a glassy carbon rotating disk electrode (RDE) or a rotating ring-disk electrode (RRDE) (Pine Research Instrumentation) coated with catalysts, a Pt auxiliary electrode and a saturated calomel reference electrode (SCE). All the potentials are reported with respect to the reversible hydrogen electrode (RHE) and all electrochemical data were obtained at room temperature. All potentials in the RHE scale were converted from the SCE scale using E (RHE) = E (SCE) + 0.99 V in 0.1 M KOH. Transmission electron microscopy (TEM) studies were performed on a TECNAI F-30 high-resolution transmission electron microscope operating at 300 kV. The samples were prepared by dropping ethanol dispersion of samples onto 300-mesh carbon-coated copper grids and immediately evaporating the solvent. X-ray diffraction (XRD) measurements were recorded on a PANalytical X'pert PRO diffractometer using Cu Kα radiation, operating at 40 kV and 30 mA. Thermogravimetric analysis (TGA) of sample was performed on a SDT-Q600 simultaneous TGA/DSC thermogravimetric analyzer (TA Instruments), and the sample was heated under air atmosphere from room temperature to 800 °C at 10 °C min^{-1}. Element analysis was performed on a Vario EL- III elemental analyzer. Surface area and pore size were determined by a surface area and porosity analyzer (Micromeritics Instrument Corp. ASAP2020). All chemicals were of analytical grade and used without further purification. Ultrapure water (Millipore, ≥18MΩ cm) was used throughout.

Synthesis of MnO-m-N-C Nanocomposite: 30 mL of aqueous solution containing 0.033 M $Mn(NO_3)_2$ and 0.033 M aniline was mixed with 30 mL of 0.033 M $KMnO_4$ aqueous solution under continuous stirring for about 30 min. The resulting solution was transferred into a 100 mL Teflon-lined stainless steel autoclave, then heated at 180 °C for 4 h, followed by natural cooling to room temperature. The precipitates were collected by centrifugation, washed with deionized water, and finally dried at 60 °C for 12 h. Then, the resulting products were carbonized into carbon-coated MnO hybrids under flowing argon at 900 °C for 4 h. Finally, the MnO-C hybrids were etched in excessive 0.1 M H_2SO_4 aqueous solution for 24 h. The resulting products were collected by centrifugation, washed with deionized water and finally dried at 60 °C for 12 h.

Synthesis of m-N-C: 250 mg of a 40 wt% aqueous dispersion of SiO_2 nanoparticles (Ludox HS40) were mixed with 30 mL of aqueous solution containing 0.1 M H_2SO_4 and 0.033 M aniline under continuous stirring for about 30 min. Then 60 mg of $(NH4)_2S_2O_8$ was added to the above solution, followed by continuous stirring about 24 h. The precipitates were collected by centrifugation, washed with deionized water, and finally dried at 60 °C for 12 h. Then, the resulting products were carbonized under flowing argon at 900 °C for 4 h. Finally, the resulting products were etched in excessive 20 wt% hydrofluoric acid to remove the silica template. The resulting products were collected by centrifugation, washed with deionized water and finally dried at 60 °C for 12 h.

Synthesis of MnO Nanoparticles: Pristine MnO nanoparticles were synthesized following a reported methodology.[50] Briefly, 4 mmol of manganese acetate was added to a mixture containing 15 mL of trioctylamine and 3 g of oleic acid at room temperature. The resulting mixture was heated rapidly to 320 °C over 15 min and maintained for 1 h under N_2 flow. Then the resulting solution was carefully cooled to 100 °C and maintained at this temperature for 1 h. The precipitates were collected by centrifugation, washed with hexane and ethanol. The capping agents on the surface of MnO nanoparticles were treated following a reported methodology.[51,52] The solid product was dispersed in *n*-butylamine and kept under stirring for 3 days and then collected by centrifugation.

Electrochemical Measurements: The RDE and RRDE were polished with 1 and 0.05 μm alumina slurry sequentially and then washed ultrasonically in water and ethanol for 15 min, respectively. Then the RDE and RRDE were subjected to potential cycling (0 to 1.1 V vs. RHE, 50 mV s^{-1}) in 0.10 M aqueous $HClO_4$ until reproducible cyclic voltammograms were obtained. 5 mg catalysts were dispersed in 5 ml ethanol, and then ultrasonicated to form a uniform black ink. The catalysts modified RDE and RRDE were prepared by cast-coating a designed volume of well-dispersed catalyst ink onto pre-polished RDE and RRDE. The catalyst loading was 100 μg cm^{-2} for each case. After drying at room temperature, 5 μL of 0.1 wt% Nafion solution was further cast-coated to form a protection layer against catalyst detaching from the electrode surface. 0.1 M KOH aqueous solution saturated with oxygen by bubbling O_2 for 30 min served as the supporting electrolyte. A flow of O_2 was maintained over the electrolyte solution for continued O_2 saturation during cyclic voltammetry experiments. In control experiments, cyclic voltammetry measurements were also performed in N_2-saturated 0.1 M KOH aqueous solution by switching a N_2 flow through the electrochemical cell. For the ORR at a RDE, the working electrode was scanned cathodically at a rate of 5 mV s^{-1} with varying rotating speed from 400 to 2500 rpm in O_2-saturated 0.1 M KOH aqueous solution. Koutecky-Levich plots were analyzed at various electrode potentials. The slopes of their linear fit lines are used to calculate the electron transfer number (*n*) on the basis of the Koutecky-Levich equation:[53]

$$\frac{1}{j} = \frac{1}{j_L} + \frac{1}{j_K} = \frac{1}{B\omega^{1/2}} + \frac{1}{j_K}$$

$$B = 0.62nFC_o D_o^{2/3} \nu^{-1/6}$$

where j is the experimentally measured current, j_L is the diffusion-limiting current, j_K is the kinetic current, ω is the angular velocity, F is the Faraday constant, C_o is the bulk concentration of O_2, and ν is the kinematic viscosity of the electrolyte. For the Tafel plot, the kinetic current was calculated from the mass-transport correction of RDE by:

$$J_K = \frac{j \times j_L}{j - j_L}$$

For the RRDE measurements, the disk electrode was scanned cathodically at a rate of 5 mV s^{-1} and the ring potential was kept at 1.5 V vs. RHE. The percentage of HO_2^- and the electron transfer number (*n*) were determined by the followed equations:[37]

$$HO_2^-\% = 200 \times \frac{i_R/N}{i_D + i_R/N}$$

$$n = 4 \times \frac{I_d}{i_d + i_r/N}$$

where I_d is the disk current, I_r is the ring current, and N is the current collection efficiency of the Pt ring. N was determined to be 0.38 from the reduction of $K_3Fe[CN]_6$, well consistent with the manufacturer's value (0.37).

Supporting Information

Supporting Information is available from the Wiley Online Library or from the author.

Acknowledgements

This work is supported by the MOST of China (2011CB932403), the NSF of China (21131005, 20925103, 21021061, 21175042), the Fok Ying Tung Education Foundation (121011), and NSF of Fujian for a Distinguished Young Investigator Grant (2009J06005). Y.M.T. also acknowledges the support of China Postdoctoral Science Foundation (20100480716). Y.M.T. and C.F.X. contributed equally to this work.

Received: May 7, 2012
Revised: June 1, 2012

---

[1] B. C. H. Steele, A. Heinzel, *Nature* **2001**, *414*, 345.
[2] J. Zhang, K. Sasaki, E. Sutter, R. R. Adzic, *Science* **2007**, *315*, 220.
[3] H. A. Gasteiger, N. M. Markovic, *Science* **2009**, *324*, 48.
[4] J. Snyder, T. Fujita, M. W. Chen, J. Erlebacher, *Nat. Mater.* **2010**, *9*, 904.
[5] V. R. Stamenkovic, B. Fowler, B. S. Mun, G. Wang, P. N. Ross, C. A. Lucas, N. M. Markovic, *Science* **2007**, *315*, 493.
[6] V. R. Stamenkovic, B. S. Mun, M. Arenz, K. J. J. Mayrhofer, C. A. Lucas, G. Wang, P. N. Ross, N. M. Markovic, *Nat. Mater.* **2007**, *6*, 241.
[7] J. Greeley, I. E. Stephens, A. S. Bondarenko, T. P. Johansson, H. A. Hansen, T. F. Jaramillo, J. Rossmeisl, I. Chorkendorff, J. K. Nørskov, *Nat. Chem.* **2009**, *1*, 552.
[8] B. Lim, M. Jiang, P. H. Camargo, E. C. Cho, J. Tao, X. Lu, Y. Zhu, Y. Xia, *Science* **2009**, *324*, 1302.
[9] R. Bashyam, P. Zelenay, *Nature* **2006**, *443*, 63.
[10] Y. Zheng, Y. Jiao, J. Chen, J. Liu, J. Liang, A. Du, W. Zhang, Z. Zhu, S. C. Smith, M. Jaroniec, G. Q. M. Lu, S. Z. Qiao, *J. Am. Chem. Soc.* **2011**, *133*, 20116.
[11] S. Yang, X. Feng, X. Wang, K. Müllen, *Angew. Chem. Int. Ed.* **2011**, *50*, 5339.
[12] Z. Yang, Z. Yao, G. Li, G. Fang, H. Nie, Z. Liu, X. Zhou, X. Chen, S. Huang, *ACS Nano* **2012**, *6*, 205.
[13] S. Wang, D. Yu, L. Dai, *J. Am. Chem. Soc.* **2011**, *133*, 5182.
[14] L. Yang, S. Jiang, Y. Zhao, L. Zhu, S. Chen, X. Wang, Q. Wu, J. Ma, Y. Ma, Z. Hu, *Angew. Chem. Int. Ed.* **2011**, *50*, 7132.
[15] D. S. Su, G. Sun, *Angew. Chem. Int. Ed.* **2011**, *50*, 11570.
[16] Y. Zheng, J. Liu, J. Liang, M. Jaroniec, S. Z. Qiao, *Energy Environ. Sci.* **2012**, *5*, 6717.
[17] K. Gong, F. Du, Z. Xia, M. Durstock, L. Dai, *Science* **2009**, *323*, 760.
[18] L. Qu, Y. Liu, J. -B. Baek., L. Dai, *ACS Nano* **2010**, *4*, 1321.

[19] J. Maruyama, N. Fukui, M. Kawaguchi, I. Abe, *J. Power Sources* **2009**, *194*, 655.
[20] Z. Chen, D. Higgins, A. Yu, L. Zhang, J. Zhang, *Energy Environ. Sci.* **2011**, *4*, 3167.
[21] M. Jahan, Q. Bao, K. P. Loh, *J. Am. Chem. Soc.* **2012**, *134*, 6707.
[22] F. Jaouen, M. Lefevre, J. P. Dodelet, M. Cai, *J. Phys. Chem. B* **2006**, *110*, 5553.
[23] L. Zhang, K. Lee, C. W. B. Bezerra, J. L. Zhang, J. J. Zhang, *Electrochim. Acta* **2009**, *54*, 6631.
[24] W. Yang, T.-P. Fellinger, M.Antonietti, *J. Am. Chem. Soc.* **2011**, *133*, 206.
[25] T. P. Fellinger, F. Hasché, P. Strasser, M. Antonietti, *J. Am. Chem. Soc.* **2012**, *134*, 4072.
[26] F. Jaouen, E. Proietti, M. Lefèvre, R. Chenitz, J.-P. Dodelet, G. Wu, H. T. Chung, C. M. Johnston, P. Zelenay, *Energy Environ. Sci.* **2011**, *4*, 114.
[27] S. Shanmugam, A. Gedanken, *J. Phys. Chem. B* **2006**, *110*, 24486.
[28] J.-S. Lee, G. S. Park, H. I. Lee, S. T. Kim, R. Cao, M. Liu, J. Cho, *Nano Lett.* **2011**, *11*, 5362.
[29] W. Xiao, D. Wang, X. W. Lou, *J. Phys. Chem. C* **2009**, *114*, 1694.
[30] Y. L. Cao, H. X. Yang, X. P. Ai, L. F. Xiao, *J. Electroanal. Chem.* **2003**, *557*, 127.
[31] F. Cheng, Y. Su, J. Liang, Z. Tao, J. Chen, *Chem. Mater.* **2009**, *22*, 898.
[32] L. Mao, D. Zhang, T. Sotomura, K. Nakatsu, N. Koshiba, T. Ohsaka, *Electrochim. Acta* **2003**, *48*, 1015.
[33] Y. Gorlin, T. F. Jaramillo, *J. Am. Chem. Soc.* **2010**, *132*, 13612.
[34] G. Wu, K. L. More, C. M. Johnston, P. Zelenay, *Science* **2011**, *332*, 443.
[35] Z. Wen, S. Ci, F. Zhang, X. Feng, S. Cui, S. Mao, S. Luo, Z. He, J. Chen, *Adv Mater.* **2012**, *24*, 1399.
[36] E. Proietti, F. Jaouen, M. Lefèvre, N. Larouche, J. Tian, J. Herranz, J. P. Dodelet, *Nat. Commun.* **2011**, *2*, 416.
[37] Y. Liang, Y. Li, H. Wang, J. Zhou, J. Wang, T. Regier, H. Dai, *Nat. Mater.* **2011**, *10*, 780.
[38] M. Lefèvre, E. Proietti, F. Jaouen, J. P. Dodelet, *Science* **2009**, *324*, 71.
[39] W. M. Zhang, P. Sherrell, A. I. Minett, J. M. Razal, J. Chen, *Energy Environ. Sci.* **2010**, *3*, 1286.
[40] R. Liu, D. Wu, X. Feng, K. Müllen, *Angew. Chem. Int. Ed.* **2010**, *49*, 2565.
[41] J. Liang, Y. Zheng, J. Chen, J. Liu, D. Hulicova-Jurcakova, M. Jaroniec, S. Z. Qiao, *Angew. Chem. Int. Ed.* **2012**, *51*, 3892.
[42] Y. F. Tang, B. L. Allen, D. R. Kauffman, A. Star, *J. Am. Chem. Soc.* **2009**, *131*, 13200.
[43] T. S. Olson, S. Pylypenko, P. Atanassov, K. Asazawa, K. Yamada, H. Tanaka, *J. Phys. Chem. C* **2010**, *114*, 5049.
[44] Z. H. Wen, J. Liu, J. H. Li, *Adv. Mater.* **2008**, *20*, 743.
[45] W. C. Choi, S. I. Woo, M. K. Jeon, J. M. Sohn, M. R. Kim, H. J. Jeon, *Adv. Mater.* **2005**, *17*, 446.
[46] M. R. Gao, Q. Gao, J. Jiang, C. H. Cui, W. T. Yao, S. H. Yu, *Angew. Chem. Int. Ed.* **2011**, *50*, 4905.
[47] Z. Wu, Y. Lv, Y. Xia, P. A. Webley, D. Zhao, *J. Am. Chem.Soc.* **2012**, *134*, 2236.
[48] S. Tominaka, S. Ohta, H. Obata, T. Momma, T. Osaka, *J. Am. Chem. Soc.* **2008**, *130*, 10456.
[49] Y. M. Tan, C. F. Xu, G. X. Chen, N. F. Zheng, Q. J. Xie, *Energy Environ. Sci.* **2012**, *5*, 6923.
[50] M. Yin, S. O'Brien, *J. Am. Chem. Soc.* **2003**, *125*, 10180.
[51] J. Wu, J. Zhang, Z. Peng, S. Yang, F. T. Wagner, H. Yang, *J. Am. Chem. Soc.* **2010**, *132*, 4984.
[52] Y. M. Tan, J. M. Fan, G. X. Chen, N. F. Zheng, Q. J. Xie, *Chem. Commun.* **2011**, *47*, 11624.
[53] *Electrochemical Methods: Fundamentals and Applications*, 2nd edition (Eds: A. J. Bard, L. R. Faulkner), Wiley, New York **2001**.